Dynamics of Hyperthermal Collisions of O(^{3}P) with CO

Amy L. Brunsvold, Hari P. Upadhyaya, Jianming Zhang, Russell Cooper, and Timothy K. Minton*

Department of Chemistry and Biochemistry, Montana State University, Bozeman, Montana 59717

Matthew Braunstein* and James W. Duff

Spectral Sciences, Incorporated, Burlington, Massachusetts 01803

Received: October 15, 2007; In Final Form: December 18, 2007

The dynamics of O(^{3}P) + CO collisions at a hyperthermal collision energy near 80 kcal mol^{-1} have been studied with a crossed molecular beams experiment and with quasi-classical trajectory calculations on computed potential energy surfaces. In the experiment, a rotatable mass spectrometer detector was used to monitor inelastically and reactively scattered products as a function of velocity and scattering angle. From these data, center-of-mass (c.m.) translational energy and angular distributions were derived for the inelastic and reactive channels. Isotopically labeled C^{18}O was used to distinguish the reactive channel (^{16}O + C^{18}O → ^{16}OC + ^{18}O) from the inelastic channel (^{16}O + C^{18}O → ^{16}O + C^{18}O). The reactive ^{16}OC molecules scattered predominantly in the forward direction, i.e., in the same direction as the velocity vector of the reagent O atoms in the c.m. frame. The c.m. translational energy distribution of the reactively scattered ^{16}OC and ^{18}O was very broad, indicating that ^{16}OC is formed with a wide range of internal energies, with an average internal excitation of ∼40% of the available energy. The c.m. translational energy distribution of the inelastically scattered C^{18}O and ^{16}O products indicated that an average of 15% of the collision energy went into internal excitation of C^{18}O, although a small fraction of the collisions transferred nearly all the collision energy into internal excitation of C^{18}O. The theoretical calculations, which extend previously published results on this system, predict c.m. translational energy and angular distributions that are in near quantitative agreement with the experimentally derived distributions. The theoretical calculations, thus validated by the experimental results, have been used to derive internal state distributions of scattered CO products and to probe in detail the interactions that lead to the observed dynamical behavior.

I. Introduction

Hyperthermal oxygen-atom collisions are abundant on and around space vehicles that travel at high velocities through the rarefied atmosphere of the Earth at altitudes of 150−700 km. In this region of the upper atmosphere, atomic oxygen (and, with a lower flux, molecular nitrogen) can collide with space vehicles and their exhaust streams at relative velocities in the vicinity of 8 km s^{-1}.[1−4] These high relative velocities may lead to gas-phase collisions with more than 100 kcal mol^{-1} of collision energy in the center-of-mass (c.m.) reference frame.[4] Such collisions may result in large energy transfers into product internal degrees of freedom and the opening of reaction channels with high barriers.

Hyperthermal collisions between O(^{3}P) and the common combustion product, CO($^1\Sigma^+$), have received a great deal of attention. When the reactants and products are in their electronic ground states, the possible outcomes of such collisions are the following:

$$\mathrm{O} + \mathrm{CO}(v, j) \rightarrow \mathrm{O} + \mathrm{CO}(v', j') \qquad \text{inelastic} \qquad \Delta H_0^\circ = 0 \quad (1)$$

$$\mathrm{O} + \mathrm{CO}(v, j) \rightarrow \mathrm{OC}(v', j') + \mathrm{O} \qquad \text{reactive} \qquad \Delta H_0^\circ = 0 \quad (2)$$

$$\mathrm{O} + \mathrm{CO}(v, j) \rightarrow \mathrm{C} + \mathrm{O}_2(v',j') \qquad \text{reactive} \qquad \Delta H_0^\circ = 256\ \text{kcal mol}^{-1} \quad (3)$$

At a typical relative velocity of 8 km s^{-1}, the c.m. collision energy of O + CO is 77.9 kcal mol^{-1}. If exhaust gases were directed at 3 km s^{-1} into the ram direction of a spacecraft, the relative velocity of O and CO could be ∼11 km s^{-1}, in which case the c.m. collision energy would be 147 kcal mol^{-1}. Achieving the collision energy needed for the formation of molecular oxygen (eq 3) would require relative velocities that are unattainable under any reasonable operating conditions. Therefore, the only channels that are accessible at the collision energies relevant to exhaust gases from space vehicles in the upper atmosphere are eqs 1 and 2. Upschulte and Caledonia[5] measured infrared emission of vibrationally excited CO following collisions between atomic oxygen and CO at relative velocities of approximately 8 km s^{-1}, and they reported a "photon excitation" cross section, $\sigma^{\mathrm{p}} = \sum_{i=1} i\sigma(v = i)$, of 7.3×10^{-17} cm^2. The definition of the photon excitation cross section reflects the nature of the photon detection measurement which weights higher vibrational levels

---

* Corresponding author. E-mail: tminton@montana.edu.

10.1021/jp710025v CCC: $40.75

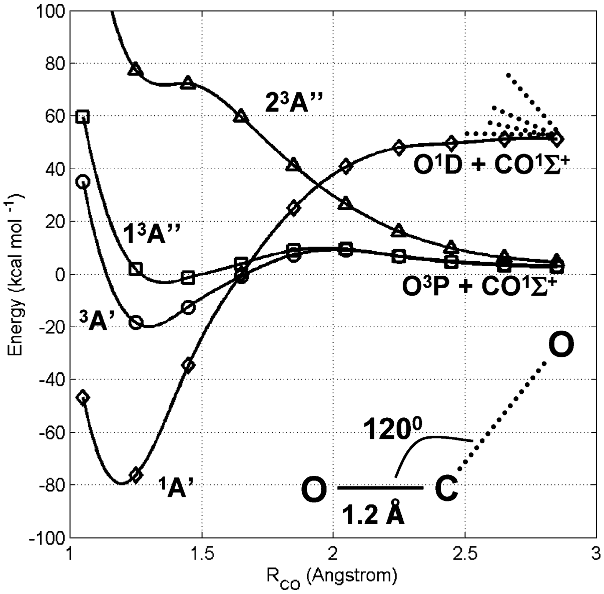

Figure 1. Calculated potential energy curves of the ground singlet state of CO_2 ($^1A'$) and the three lowest triplet states, $^3A'$, $1^3A''$, and $2^3A''$, at an O−C−O angle of 120° and where one of the C−O bond distances is fixed at 1.2 Å and the other is varied. The curves show these states, at C_s geometries to their O + CO dissociation limits, as a function of the variable C−O distance, R_{CO}.

approximately linearly, in line with the general behavior of diatomic molecular Einstein coefficients for vibrational decay. From their measured spectra, they concluded that the CO molecules were highly vibrationally excited, up to CO($v = 11$). Their result presumably contained contributions from both inelastic and reactive scattering. A space-based study by Green et al.,[6] where optical emission spectra were measured from a remote spacecraft after CO gas was released from a canister in low-Earth orbit, determined that bright infrared emissions in both fundamental and overtone vibrational bands resulted from the highly energetic interaction of the released CO with ambient O(^{3}P) at relative velocities of ~8 km s^{-1}. Their measured spectra showed substantial rotational and vibrational excitation in the CO product, closely matching the results of Upschulte and Caledonia. Green et al.[6] estimated the photon excitation cross section to be on the order of 10^{-16} cm^2, in reasonable agreement with the results of Upschulte and Caledonia.

Braunstein and Duff[7] computed the potential energy surfaces of the three lowest electronic triplet states of CO_2 (one $^3A'$ state and two $^3A''$ states), which correlate with O(^{3}P) + CO($^1\Sigma^+$). In addition, they ran classical trajectories on these surfaces. Figure 1 shows the calculated potential energy curves of the ground singlet state of CO_2($^1A'$) and the three lowest triplet states, with the O−C−O angle equal to 120°. The energy shown here is a function of one of the CO bond lengths, while the length of the other CO bond is fixed at 1.2 Å. For the lowest triplet state at its transition state geometry, which is slightly different than shown in the figure, the barrier to O-atom exchange, eq 2, was calculated to be 4.6 kcal mol^{-1}. Although coupling to the singlet ground state is spin-forbidden from the three lowest-lying triplet states, the singlet potential energy surface (the ground state of CO_2, $X^1\Sigma_g^+$) crosses the triplet surfaces and leads to a higher dissociation limit, with products, O(^{1}D) + CO($^1\Sigma^+$), about 46 kcal mol^{-1} above the dissociation limit that leads to O(^{3}P) + CO($^1\Sigma^+$). Intersystem crossing (ISC) is thus possible, although spin conservation is generally favored for systems containing first-row atoms, and other studies involving hyperthermal O-atom reactions showed no evidence of ISC.[8,9] Quasi-classical trajectory (QCT) calculations on the computed triplet surfaces which did not include isc effects[7] agreed well with available kinetic data on vibrational relaxation of CO($v = 1 \rightarrow v = 0$) by O(^{3}P), except at low temperature. The shape of the emission spectra of CO based on the calculations for collisions at a relative velocity of 8 km s^{-1} was in fair agreement with the experimental observations of Upschulte and Caledonia and with the spaced-based observations of Green et al. However, the magnitude of the calculated photon excitation function for CO was about an order of magnitude above the two experimental values (see Figure 6 of ref 7). A subsequent modeling study[10] suggested that the difference in cross sections between the measurement of Upschulte and Caledonia and the calculations of Braunstein and Duff was the result of multiple-collision effects. However, a linear dependence of the measured experimental signal suggested single-collision conditions, and the cross section differences between theory and experiment have not been fully explained. The calculated trajectories were studied to learn mechanistic details of the collisions that lead to vibrational excitation through inelastic and reactive collisions. It was found that these processes occur when the reagent O atom approaches the carbon end of CO on the two low-lying triplet surfaces, $^3A'$ and $1^3A''$, which have small wells, at O−C−O angles between 80° and 140°.

We describe here a combined theoretical and crossed molecular beams study of O(^{3}P) + CO collisions at a hyperthermal collision energy near 80 kcal mol^{-1} (E_{coll} = 77.9 kcal mol^{-1} for the theoretical calculations and $\langle E_{coll} \rangle$ = 83 kcal mol^{-1} for the experiment). Isotopic substitution was used in the experiment to distinguish between the reactive channel, $^{16}O + C^{18}O \rightarrow {}^{16}OC + {}^{18}O$, eq 2, and the inelastic channel, $^{16}O + C^{18}O \rightarrow {}^{16}O + C^{18}O$, eq 1. We investigated the dynamics of the reactive and inelastic pathways, including the disposal of energy in the products and the angular distributions of the scattered products. With the use of the surfaces of ref 7, new QCT calculations were performed which extend previous results in order to facilitate direct comparisons with the present measurements and to explore more fully the dynamics. The results of the QCT calculations are in almost quantitative agreement with the present experimental data.

II. Theoretical Details

II.A. Methods. The theoretical methods are based on the potential surfaces and QCT procedures of Braunstein and Duff.[7] We used the same surfaces of Braunstein and Duff, and we extended the QCT calculations to generate new cross section results that can be compared directly with the experimental data discussed in this paper and at several collision energies well below and above those used in the experiment. The present work provides new and extensive results that separate the reactive and inelastic cross sections. The present work also uses at least an order of magnitude more trajectories per collision energy than the earlier work, allowing for improved statistical convergence.

II.A.1. Potential Energy Surfaces. We briefly review the key features of the potential energy surfaces used. Complete details can be found elsewhere.[7] Figure 1 shows the basic features of the relevant potentials. Collisions of O(^{3}P) with CO($^1\Sigma^+$) correlate to three electronic states of CO_2, all triplets: one $^3A'$ state and two $^3A''$ states. The five nearby singlet states, which can only participate through weak spin−orbit interactions, lead to O(^{1}D) and CO($^1\Sigma^+$), about 46 kcal mol^{-1} above the O(^{3}P) + CO($^1\Sigma^+$) threshold. One of these five singlet states leads to the $^1\Sigma_g^+$ ground state of CO_2 about 127 kcal mol^{-1} below the O(^{3}P)

+ CO($^1\Sigma^+$) threshold. The remainder are relatively high in energy and give rise to some of the complex features in the CO_2 UV photoabsorption spectrum starting about 23 kcal mol^{-1} above the O(^{3}P) + CO($^1\Sigma^+$) threshold.[11] As in our earlier work,[7] we ignored spin−orbit interactions that could mix the singlet and triplet states.

The potentials used are global fits of ∼320 separate ab initio calculations of the three lowest triplet states of CO_2. The ab initio calculations were performed at the (12 electron, 10 orbital) CASSCF-MP2 level, within a modest 631+G(d) basis set, with the electronic structure code GAMESS.[12] The lowest two states, $^3A'$ and $1^3A''$, have well depths of 21.7 and 5.07 kcal mol^{-1}, respectively. These minima occur near the geometries shown in Figure 1. For the $^3A'$ state, the minimum occurs at $r_1 = r_2 =$ 1.26 Å, $\theta = 118°$, and for the $1^3A''$ state, the minimum occurs at $r_1 = r_2 = 1.27$ Å, $\theta = 127°$. The $2^3A''$ state is mostly repulsive and has a saddle point with C_{2v} geometry. The $^3A'$ and $1^3A''$ states have small barriers of 4.6 and 6.9 kcal mol^{-1}, respectively, which occur at C_s geometries of their transition states near to those shown in Figure 1. For the $^3A'$ state, the transition state geometry is $r_1 = 1.16$ Å, $r_2 = 2.0$ Å, $\theta = 112°$, and for the $1^3A''$ state, the transition state geometry is $r_1 =$ 1.16 Å, $r_2 = 1.85$ Å, $\theta = 122°$. The ab initio points of the three electronic states were globally fit with the method of Aguado and Paniagua.[13]

II.A.2. Dynamics and Cross Sections. The three lowest triplet potential energy surfaces were used to generate cross sections at several fixed collision energies. Each potential surface was treated independently, and total cross sections were obtained by weighting the contribution of each electronic state by one-third: $\sigma = {}^1/_3[\sigma(^3A') + \sigma(1^3A'') + \sigma(2^3A'')]$. We used standard Monte Carlo methods[14] to generate QCT cross sections, separating contributions into reactive collisions, where the incoming O atom is exchanged with the O atom belonging to the target CO, and inelastic collisions, where the incoming O atom is not exchanged with the O atom belonging to the target CO. For a trajectory to contribute to the inelastic cross section, the final CO(v', j') state must be different than the initial CO(v, j) state. We note that all three electronic states will have significant contributions to the inelastic cross sections. The $2^3A''$ state will in general have only minor contributions to the reactive cross sections because of its repulsive nature. The lowest two electronic states, $^3A'$ and $1^3A''$, will have major contributions to the reactive cross sections because of their low barriers to reaction. All calculations were performed with ^{12}C and ^{16}O atom masses for the target CO and ^{16}O for the incoming O atom. The CO mass used in the calculations is therefore slightly different from the experimental measurements, which used ^{16}O + $^{12}C^{18}O$. However, at relative collision velocities of ∼8 km s^{-1}, we believe that differences in results arising from the mass difference between $^{12}C^{16}O$ and $^{12}C^{18}O$ are much smaller than other approximations made in the present calculations. All calculations were done with the target CO in the ground vibrational state and a rotational temperature of 300 K.

We performed two sets of QCT calculations. In one set we focused on obtaining results that could be directly compared with the present measurements. We set the collision velocity to 8 km s^{-1} (77.9 kcal mol^{-1}). The maximum impact parameter was set to 10 au (5.29 Å), and 1×10^6 trajectories were run for each of the three electronic states. The value of the maximum impact parameter was made relatively large in order capture the low-angle, low-energy (rotational) scattering in the inelastic channel, which is important when comparing to the present measurements. We calculated differential angular cross sections,

$$\frac{d\sigma}{d\Omega} = \pi b_{\max}^2 \frac{N^{\Delta\theta}}{N_{\mathrm{tot}}} \frac{1}{2\pi(\sin\theta)\Delta\theta}$$

where $b_{\max}$ is the maximum impact parameter, $N^{\Delta\theta}$ is the number of trajectories within the angular bin, $\Delta\theta$, and N_{tot} is the total number of trajectories. To compare with the fine angular resolution of the present measurements, we set $\Delta\theta = 2°$. As discussed in detail later, for the reactive channel, the c.m. scattering angle θ is taken to be the angle between the c.m. velocity vector of the reagent O atom and the c.m. velocity vector of the product CO. For the inelastic channel, θ is the angle between the c.m. velocity vector of the reagent O atom and the c.m. velocity vector of the product O atom. We also calculated c.m. differential translational energy cross sections,

$$\frac{d\sigma}{dE_{\mathrm{trans}}} = \pi b_{\max}^2 \frac{N^{\Delta E\mathrm{trans}}}{N_{\mathrm{tot}}} \frac{1}{\Delta E_{\mathrm{trans}}}$$

where $N^{\Delta E\mathrm{trans}}$ is the number of trajectories with a final product translational energy, E_{trans}, within an energy bin, $\Delta E_{\mathrm{trans}}$. We used an energy bin width of 5.8 kcal mol^{-1}, which approximates the experimental translational energy resolution.

In a second set of QCT calculations, we focused on the collision energy dependence of the rovibrationally resolved cross sections. We performed QCT calculations at O + CO collision velocities of 3, 4, 5, 6, 7, 8, 9, and 10 km s^{-1}, corresponding to c.m. collision energies of 11.0, 19.5, 30.4, 43.8, 59.6, 77.9, 99.6, and 121.7 kcal mol^{-1}, respectively, with the maximum impact parameter set to 5 au (2.65 Å). The maximum impact parameter of 5 au used in these calculations is not adequate to capture low-angle inelastic scattering resulting in CO($v = 0$) products (pure rotational transitions). However, these calculations should be sufficient for all reactive collisions and inelastic collisions leading to CO vibrational excitation. In this set of calculations, 2.5×10^5 trajectories were run for each electronic state at each collision energy. This number of trajectories is about a factor of 10 larger than used in our earlier study.[7] In all calculations, standard histogram binning was used.

II.B. Theoretical Results. *II.B.1. Results for 8 km s^{-1} Collision Velocity.* Figure 2 shows the calculated results for the differential product translational energy, E_{trans}, cross sections for reactive, eq 2, and inelastic, eq 1, channels of O + CO collisions at a relative velocity of 8 km s^{-1} (77.9 kcal mol^{-1}). The reactive and inelastic distributions are shown with (solid lines) and without (dashed lines) the contribution of product CO($v = 0$), in order to separate the dynamics of pure rotational excitation, which dominates the inelastic channel at high translational energies, from vibrational excitation. The energy bin width is equal to 5.8 kcal mol^{-1} starting at a center bin of 2.9 kcal mol^{-1} so that these theoretical results are directly comparable to the present measured distributions, which have a similar resolution. Distributions obtained after state-resolved binning the product CO(v, j) states, discussed further below, should reveal detailed structure corresponding to rovibrationally resolved CO. We note that the highest energy nonzero cross sections extend to the translational energy bin centered on 83.7 kcal mol^{-1}, which is above the collision energy. Because the reagent CO is at 300 K, some initial rotational energy ends up in product translation for a small fraction of the collisions, and there is some leakage into this high-energy bin.

In Figure 2, a large product translational energy, E_{trans}, corresponds to a low product internal energy. The peak and

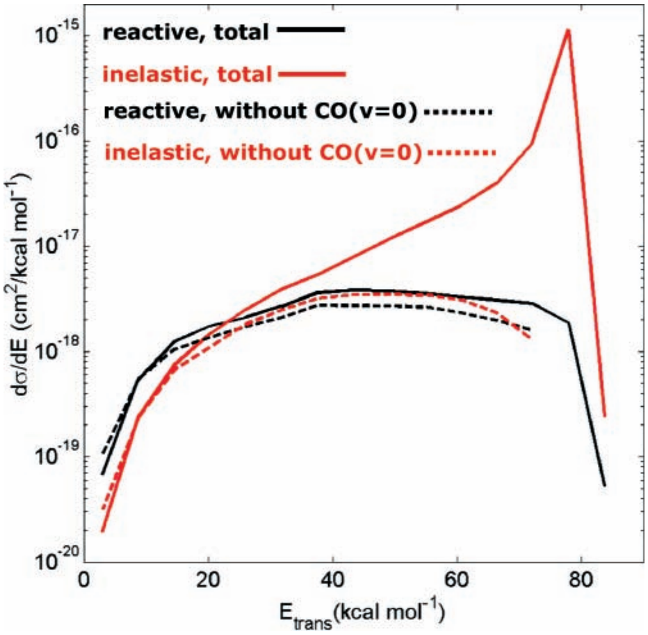

Figure 2. Calculated differential energy cross sections, dσ/dE_{trans}, for O + CO collisions at 8 km s^{-1} collision velocity (E_{coll} = 77.9 kcal mol^{-1}), where E_{trans} is the total product translational energy in the center-of-mass (c.m.) frame: (black line) total reactive channel; (red line) total inelastic channel; (black dashed line) total reactive minus contribution from reactive CO(v = 0) product; (red dashed line) total inelastic minus contribution from inelastic CO(v = 0) product.

general behavior at high E_{trans} for the inelastic channel corresponds to mostly pure rotational excitation, and it is typical of nonreactive collisions that occur on a repulsive potential. At lower E_{trans} (higher CO product internal energy), particularly below E_{trans} = 40 kcal mol^{-1}, the reactive and inelastic channels have the same broad and flat shape and nearly the same magnitude. The appreciable value of the differential cross section persists nearly to the zero translational energy cutoff, corresponding to all the available collision energy going into CO internal energy. Also shown are the reactive and inelastic differential translational energy cross sections with the contribution from the product CO(v = 0) removed, i.e., all trajectories where the product CO is in the vibrational ground state do not contribute. The reactive and inelastic channels with the CO(v = 0) contribution removed are nearly identical for all energies and track the full reactive channel (including the CO(v = 0) contribution) differential cross sections below about $E_{\text{trans}} \sim 70$ kcal mol^{-1}, which is the approximate threshold for creating vibrationally excited CO. This result implies that the underlying dynamics for collision products where CO is vibrationally excited are similar for both the reactive and inelastic channels.

Figure 3 shows the calculated differential angular cross section for O + CO collisions at 8 km s^{-1} collision velocity for the reactive, eq 2, and inelastic channels, eq 1. Results are shown both with (solid lines) and without (dashed lines) the product CO(v = 0) contribution, in order to separate pure rotational excitation from rovibrational excitation. Use of a relatively small angular bin width of 2° reveals small rapid oscillations in these curves for smaller values of the cross sections, which is an indication of the statistical uncertainty of these results. In Figure 3, the large values at low angles for the inelastic channel are typical of low-angle, low-energy-transfer collisions on repulsive surfaces. The peak at low angle for the reactive channel suggests a mechanism where the incoming O atom reacts with the carbon atom on the target CO, and the product CO is scattered mostly forward, i.e., in the same direction as the reagent O-atom velocity vector. Thus, whether it reacts or is scattered inelastically, the reagent O atom is scattered mostly in the same direction as its initial velocity vector. A major contributing factor to this forward scattering is the preferred angle of approach for O with CO, which for reactive and highly inelastic collisions corresponds to an O−C−O angle near 130°. As seen in the polar plots of the O−C−O potential for the ground ^{3}A′ state (see Figure 3 of ref 7; the second electronic surface is similar), other angles of approach are repulsive up to high energies. The bent angle of approach allows the O atom to penetrate close to the C atom of the target CO and either form a new bond (i.e., react) or otherwise excite the target CO. In either case, the product CO or the inelastically scattered O atom tends to proceed in the direction that the reagent O atom was traveling. The favored angles of approach are also close to the transition state geometries near 120°. The differential angular cross section for the reactive channel is broad as a function of scattering angle, with a small backward peak near 180°. Also shown are the differential angular cross sections without the CO(v = 0) contributions. The reactive and inelastic cross sections without the CO(v = 0) contributions are again very similar and closely approximate the full reactive differential cross section. It is likely that for vibrational excitation, reactive and inelastic trajectories follow similar initial paths and end up either on the reagent side of the transition state barrier for inelastic collisions or on the product side of the transition state barrier for reactive collisions (see Figure 12 of ref 7).

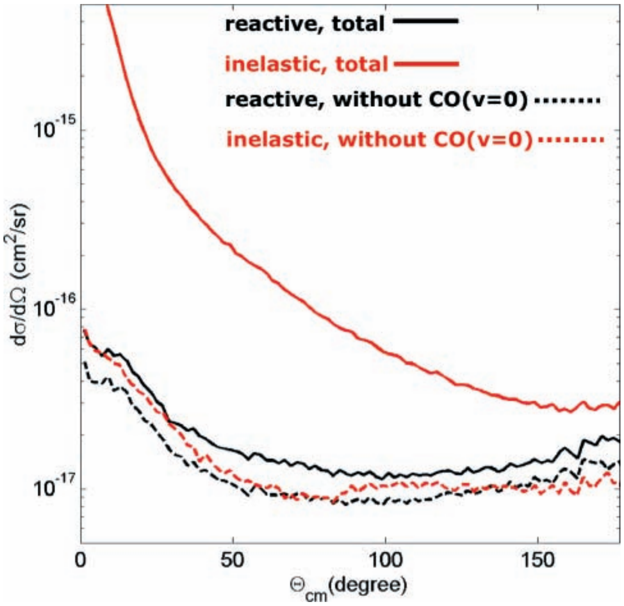

Figure 3. Calculated differential angular cross sections, dσ/dΩ, for O + CO collisions in the c.m. frame at 8 km s^{-1} collision velocity (E_{coll} = 77.9 kcal mol^{-1}): (black line) total reactive channel; (red line) total inelastic channel; (black dashed line) total reactive minus contribution from reactive CO(v = 0) product; (red dashed line), total inelastic minus contribution from inelastic CO(v = 0) product. For the reactive channel, the c.m. scattering angle, Θ_{cm}, is defined as the inverse cosine of the dot product of the unit velocity vectors in the c.m. frame of the incoming (reagent) O atom and outgoing (product) CO molecule. For the inelastic channel, the c.m. scattering angle, Θ_{cm}, is defined as the inverse cosine of the dot product of the unit velocity vectors in the c.m. frame of the incoming (reagent) O atom and outgoing (product) O atom.

Figure 4a−c shows the reactive (Figure 4a) and inelastic, with (Figure 4b) and without (Figure 4c) the product CO(v = 0) contribution, rovibrationally resolved cross sections versus the product translational energy. The values of E_{trans} in these plots were obtained by E_{trans} = 77.9 kcal mol^{-1} − E_{internal}(CO(v, j)).

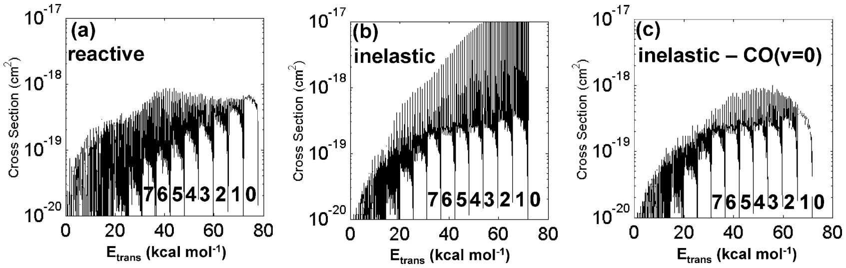

Figure 4. Calculated cross sections for O + CO collisions at 8 km s^{-1} collision velocity ($E_{\rm coll}$ = 77.9 kcal mol^{-1}), showing the contribution from each final CO(v, j) state as a function of the final translational energy of collision products: (a) reactive channel; (b) inelastic channel; (c) inelastic channel minus the CO(v = 0, j) product contributions. The numbers in the figures indicate the thresholds for the CO(v) product vibrational levels. In (b), the contribution from CO(v = 0) below the CO(v = 1) threshold extends above the axis limit and so is not visible in the figure.

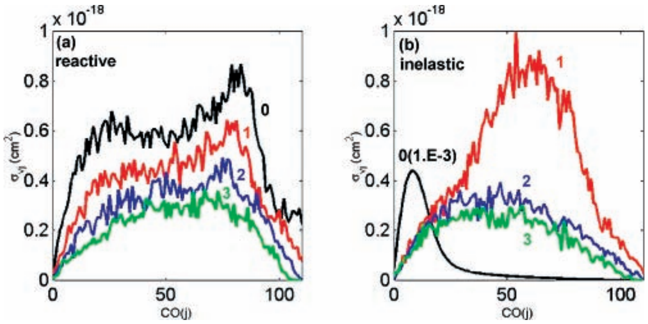

Figure 5. Calculated rovibrationally resolved cross sections for O + CO collisions at 8 km s^{-1} collision velocity ($E_{\rm coll}$ = 77.9 kcal mol^{-1}): (a) reactive channel; (b) inelastic channel; (black line) CO(v = 0); (red line) CO(v = 1); (blue line) CO(v = 2); (green line) CO(v = 3). The CO(v = 0) inelastic cross section has been multiplied by 1 × 10^{-3} in order to fit on the scale.

The numbers in Figure 4a−c (0−7) correspond to CO(v) level thresholds. (The $\sigma(v, j = 0)$ cross sections dip down to very low values and so conveniently indicate vibrational level onsets.) For the inelastic cross sections in Figure 4b, much of the v = 0 cross section is above the scale of the figure. Our expression for $E_{\rm trans}$ neglects a small energy contribution from the initial reagent CO internal energy. We note also that the cross section is obtained after binning the classical trajectories into quantum states. Therefore, these finely resolved cross sections cannot be compared quantitatively to the differential translational energy cross sections shown in Figure 2. However, they are nearly the same quantity, and they reveal rich and detailed state populations. As we shall show, product CO vibrational excitation for $v > 10$ and $j > 100$ is seen in the calculations. Many of these CO(v, j) states are evident in Figure 4, but many of the higher (v, j) states overlap the thresholds of higher vibrational manifolds, making these states difficult to distinguish from one another. This rich structure resulting from the highly excited-state populations shown in Figure 4 underlies the results of Figure 2 and could possibly be revealed in very highly resolved energy measurements. As seen in Figure 2, the overall magnitude and shape of the inelastic rovibrationally resolved cross sections without the product (CO(v = 0)) contribution, Figure 4c, closely resemble the full reactive rovibrational distribution, Figure 4a. The largest differences occur at extremely low $E_{\rm trans}$ (high CO internal energy) where the reactive cross sections remain fairly large up until the $E_{\rm trans}$ = 0 cutoff.

Figure 5 shows the reactive (Figure 5a) and inelastic (Figure 5b) rovibrationally resolved cross section σ(CO(v, j)), for O + CO collisions at 8 km s^{-1}, for v = 0−3. We have multiplied the $\sigma(0, j)$ inelastic cross sections by 1 × 10^{-3} to put these data on a common scale. The rapid oscillations in the other curves are an indication of the statistical uncertainty in the Monte Carlo calculations. The reactive cross sections for each vibrational level have similar broad shapes, with single maxima, that extend to the maximum available energy, except for $\sigma(0, j)$ which has two maxima, one at high j and one at low j. For $\sigma(v > 0, j)$ taken together, the reactive rotational distributions can be fit well with a Boltzmann rotational distribution of ~8000 K. (The vibrational temperature is also near 8000 K.) The rovibrationally resolved cross sections persist to very high rotational quantum numbers, up to $j \sim 110$ (corresponding to ~65 kcal mol^{-1}), which is an appreciable fraction of the collision energy of 77.9 kcal mol^{-1}. The inelastic rovibrationally resolved cross sections for product CO($v > 0$) have a similar broad shape as the reactive cross sections, extending to $j \sim 100$.

II.B.2. Results at Collision Velocities from 3 through 10 km s^{-1}. To gain more insight into the dynamics, and in anticipation of possible future experiments, Figure 6 shows the vibrationally resolved cross sections, for O + CO reactive and inelastic collisions at 3, 4, 5, 6, 7, 8, 9, and 10 km s^{-1} collision velocities. The inelastic $\sigma(v = 0)$ cross section is above the scale of the figure. Except for the highest vibrational populations near the available energy limit for a particular collision velocity, the reactive vibrational distributions are similar to Boltzmann distributions. The effective temperatures of these distributions increase with approximately the square of the collision velocity. The inelastic, vibrationally resolved cross sections closely resemble the reactive vibrationally resolved cross sections except for $\sigma(v = 0)$. For the present energy-dependent results, which focus on CO vibrational excitation and where the maximum impact parameter is 5 au, the $\sigma(v = 0)$ inelastic results will not include significant contributions from large-impact-parameter, small ΔJ transitions. For vibrationally excited products, the inelastic CO distributions are slightly hotter than the reactive distributions.

Figure 7 examines the average rotational and vibrational energies of product CO, where we show the rotational and vibrational energy fractions, $f^{\,j}$ and $f^{\,v}$, respectively, for O + CO reactive and inelastic collisions at 3, 4, 5, 6, 7, 8, 9, and 10 km s^{-1} collision velocities. The rotational and vibrational energy fractions are defined as follows:

$$f^{\,j} = \left\langle \frac{E_j}{E_{\rm collision}} \right\rangle = \frac{1}{E_{\rm collision}} \left[\frac{1}{\sigma_{\rm tot}} \sum_j E_j \sigma_j \right]$$

$$f^{\,v} = \left\langle \frac{E_v}{E_{\rm collision}} \right\rangle = \frac{1}{E_{\rm collision}} \left[\frac{1}{\sigma_{\rm tot}} \sum_v E_v \sigma_v \right]$$

where E_j is the rotational energy, E_v is the vibrational energy, $E_{\rm collision}$ is the collision energy, $\sigma_{\rm tot}$ is the total cross section, $\sigma_{\rm tot} = \sum_{v,j} \sigma(v, j)$, $\sigma(j) = \sum_v \sigma(v, j)$, and $\sigma(v) = \sum_j \sigma(v, j)$. The vibrational energy fraction increases with collision energy for

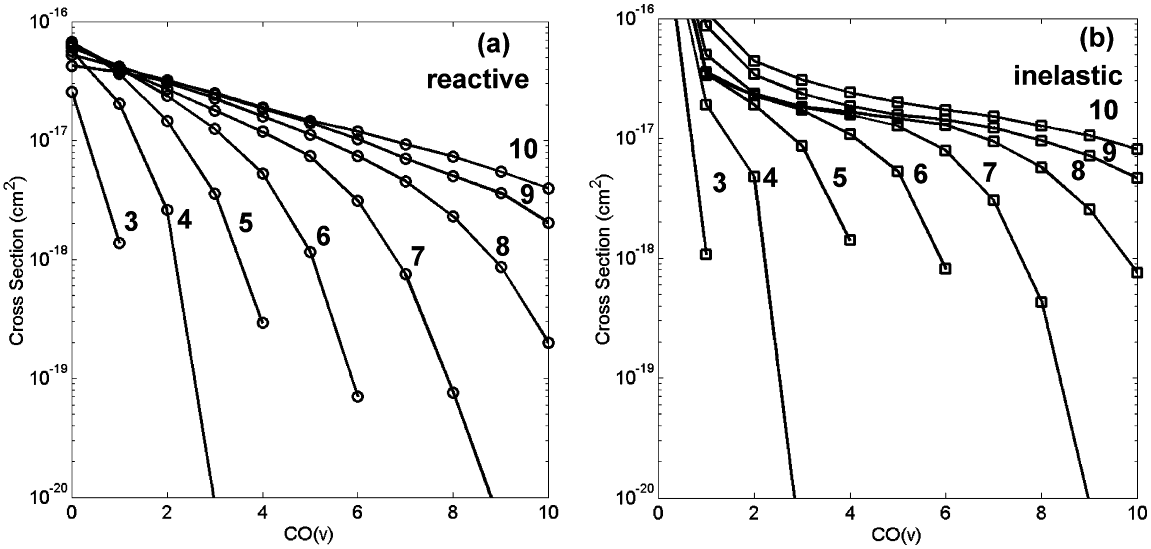

Figure 6. Calculated vibrationally resolved cross sections for O + CO collisions at 3, 4, 5, 6, 7, 8, 9, and 10 km s^{-1} collision velocities: (a) reactive collisions; (b) inelastic collisions. The numbers in the figure refer to the collision velocity.

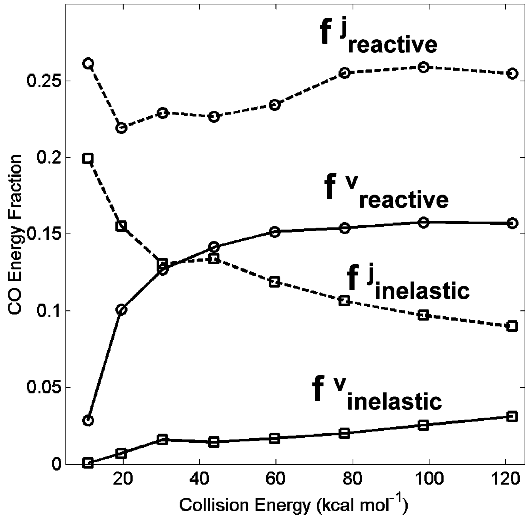

Figure 7. Calculated CO product energy fractions for O + CO collisions as a function of collision energy: (○) reactive channel; (□) inelastic channel; (—) vibrational energy fraction (f^v); (− − −) rotational energy fraction (f^j).

the reactive and inelastic channels. The reactive energy fraction shows a rapid increase from threshold, which may reflect the small energy barrier to reaction. The large $\sigma(v = 0)$ inelastic cross section makes the overall inelastic vibrational energy fraction, which is an average of the energy of vibrational states, smaller than the reactive energy fraction. The reactive rotational energy fraction is generally flat, whereas the inelastic rotational energy fraction decreases with collision energy. For collision velocities above 8 km s^{-1}, the distribution of internal energy in the inelastic channel continues to change, but it remains relatively constant in the reactive channel.

Figure 8 shows two different excitation functions for O + CO collisions: a photon excitation function, σ^p, and a vibrational excitation function, σ^e, both as a function of collision energy. These excitation functions are separated into reactive and inelastic components. It is useful to examine the photon excitation function $\sigma^p = \sum_{i=1} i\sigma(v = i)$. The photon excitation function is particularly convenient for comparisons to laboratory measurements of photon production due to O + CO collisions which integrate signal over the entire fundamental CO band from 4 to 7 μm, such as the measurements of Upschulte and Caledonia.[5] The photon excitation function also provides a way to compare directly reactive and inelastic excitation functions by not including CO products formed in the vibrational ground state, which for the inelastic channel would otherwise mask the behavior of the vibrationally excited CO cross section. The photon excitation functions for the reactive and inelastic channels are nearly the same, with the inelastic channel slightly larger. This behavior reflects the similarity of the underlying vibrationally resolved cross sections for excited CO products. We define the vibrational excitation function as $\sigma^e = \sum_{i=1} \sigma(v = i)$. The vibrational excitation functions are also very similar.

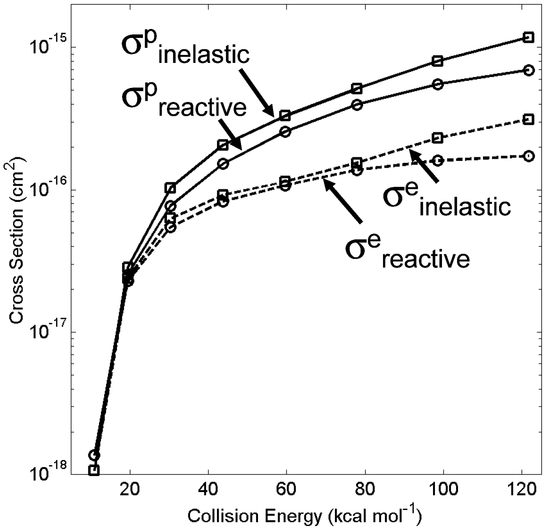

Figure 8. Calculated vibrational excitation and photon cross sections for O + CO collisions as a function of collision energy: (○) reactive channel; (□) inelastic channel; (—) results for the photon cross section $\sigma^p = \sigma(v = 1) + 2\sigma(v = 2) + 3\sigma(v = 3) + ...$; (− − −) results for the vibrational excitation function $\sigma^e = \sigma(v = 1) + \sigma(v = 2) + \sigma(v = 3) + ...$

III. Experimental Details

III.A. Methods. The experiments were performed with the use of a crossed molecular beams apparatus (see Figure 9) equipped with a fast-atom beam source.[8,15−18] General details about the experimental apparatus and the analysis can be found in an earlier paper.[8] A pulsed beam of oxygen atoms (^{16}O) was

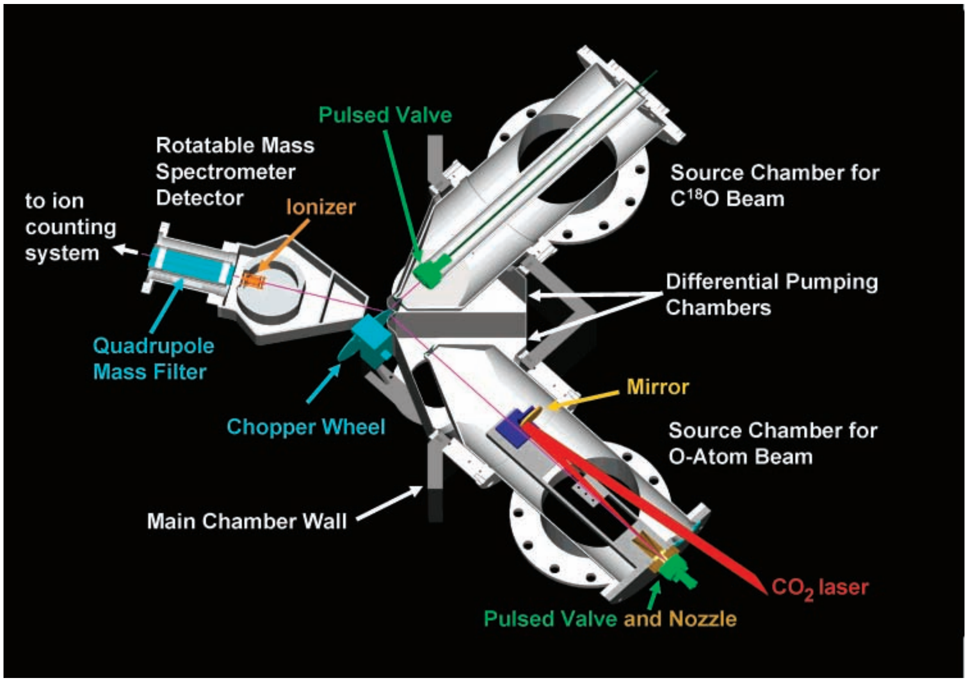

Figure 9. Pictorial diagram of the crossed molecular beams apparatus.

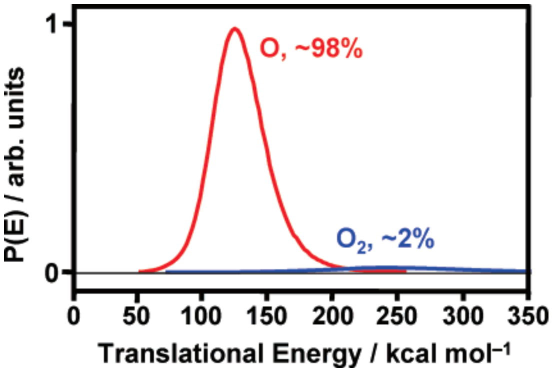

Figure 10. Translational energy distributions of atomic and molecular oxygen in the hyperthermal beam. The average translational energy of the O atoms in the beam is 125.5 kcal mol^{-1}. The mole fraction of O atoms is 98%, and the mole fraction of O_2 molecules is 2%.

crossed at right angles with a pulsed, supersonic beam of $^{12}C^{18}O$ gas. Products that scattered from the interaction region were detected with a rotatable mass spectrometer detector that measured number-density distributions as a function of arrival time at the electron-bombardment ionizer, $N(t)$. These number-density distributions are commonly referred to as time-of-flight (TOF) distributions. Laboratory angular distributions, $N(\Theta)$, where Θ is the laboratory angle of the scattered products with respect to the O-atom beam, are determined by integrating the TOF distributions over time at a fixed angle for a series of laboratory angles, Θ. These data are collected in the laboratory reference frame, so a forward-convolution method[8,19,20] is employed to derive c.m. quantities from the laboratory TOF and angular distributions.

The hyperthermal beam used in the experiment had an average translational energy of 125.5 kcal mol^{-1} (Figure 10), which corresponds to a velocity of 8100 m s^{-1}. The mole fraction of atomic oxygen in the beam was approximately 98%. The hyperthermal ^{16}O-atom beam was crossed at a 90° intersection angle by a pulsed beam of isotopically labeled carbon monoxide molecules ($C^{18}O$). The $C^{18}O$ (Isotec, Sigma Aldrich) was 98.7% $C^{18}O$, with the remainder (1.3%) being $C^{16}O$. A supersonic expansion of $C^{18}O$ was created with a piezoelectric pulsed valve from a stagnation pressure of 10 psig $C^{18}O$.[21] The $C^{18}O$ beam passed through a 5 mm diameter skimmer and a 3 mm diameter aperture before crossing the O-atom beam. The distance between the nozzle and skimmer was 9.2 cm, and the distance from the skimmer to the 3 mm diameter aperture was 2.8 cm. From the aperture, the beam traveled 1.5 cm to the crossing point of the two beams. The $C^{18}O$ beam velocity was estimated to be 800 ± 80 m s^{-1}.[22] The velocity of the $C^{18}O$ beam was an order of magnitude lower than that of the O-atom beam, and the velocity width of the $C^{18}O$ beam was not considered in the analysis of the experimental data. The crossing region of the two beams was located 99 cm from the apex of the conical nozzle of the O-atom source and 13 cm from the orifice of the $C^{18}O$ pulsed valve source.

The collision-energy distribution in the c.m. reference frame was derived from the O-atom beam-velocity distribution (related to Figure 10 by $E_{\mathrm{trans}} = {}^1/_2 m v^2$) and the nominal velocity of the carbon monoxide beam using the equation $E_{\mathrm{coll}} = {}^1/_2 \mu v_{\mathrm{rel}}^2$, where μ is the reduced mass and v_{rel} is the relative velocity of the O atoms and the $C^{18}O$ molecules. The average collision energy in this experiment was 83 kcal mol^{-1}, and the width of the collision-energy distribution (full width at half-maximum) was ~30 kcal mol^{-1}, ranging from 70 to 100 kcal mol^{-1}.[23] A Newton diagram for collisions of O atoms and $C^{18}O$ with $E_{\mathrm{coll}} = 83$ kcal mol^{-1} is shown in Figure 11. This diagram shows maximum recoil velocities for inelastically scattered $C^{18}O$ (solid blue circle) and ^{16}O (dashed blue circle). It also shows maximum recoil velocities for reactively scattered ^{16}OC (solid red circle) and ^{18}O (dashed red circles). The shaded region shown on the Newton diagram indicates the range of laboratory angles used for the experiment: 6−54° with respect to the nominal velocity vector of the hyperthermal O-atom beam.

The experiments focused on the reactively scattered ^{16}OC molecules (detected at $m/z = 28$), inelastically scattered $C^{18}O$ molecules (detected at $m/z = 30$), and inelastically scattered O atoms (detected at $m/z = 16$). Signals from $m/z = 32$ (O_2^+) were used to correct the $m/z = 16$ data for the contribution of inelastically scattered O_2 cracking to O^+ in the ionizer. Low

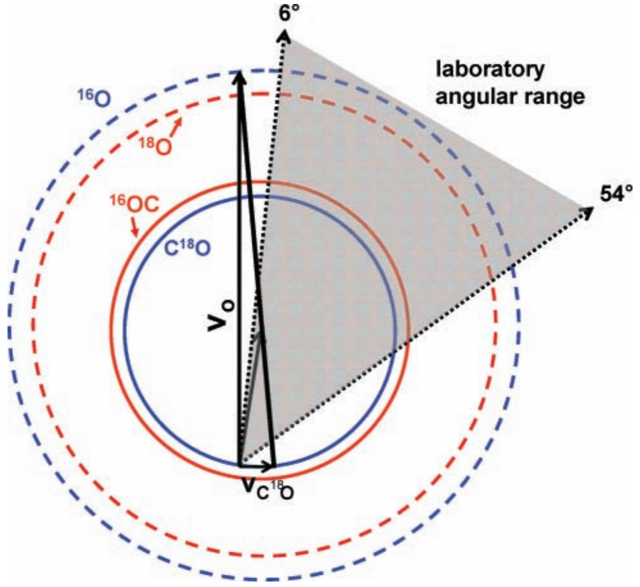

Figure 11. Newton diagram for collisions of O(^{3}P) with C^{18}O at E_{coll} = 83 kcal mol^{-1}, where O has a velocity of 8100 m s^{-1} and the C^{18}O beam velocity is 800 m s^{-1}. The shaded region indicates the range of laboratory angles examined. The radii of the blue circles represent the recoil velocities of elastically scattered C^{18}O (solid) and ^{16}O (dashed). The radii of the red circles represent the maximum recoil velocities of reactively scattered ^{16}OC (solid) and ^{18}O (dashed).

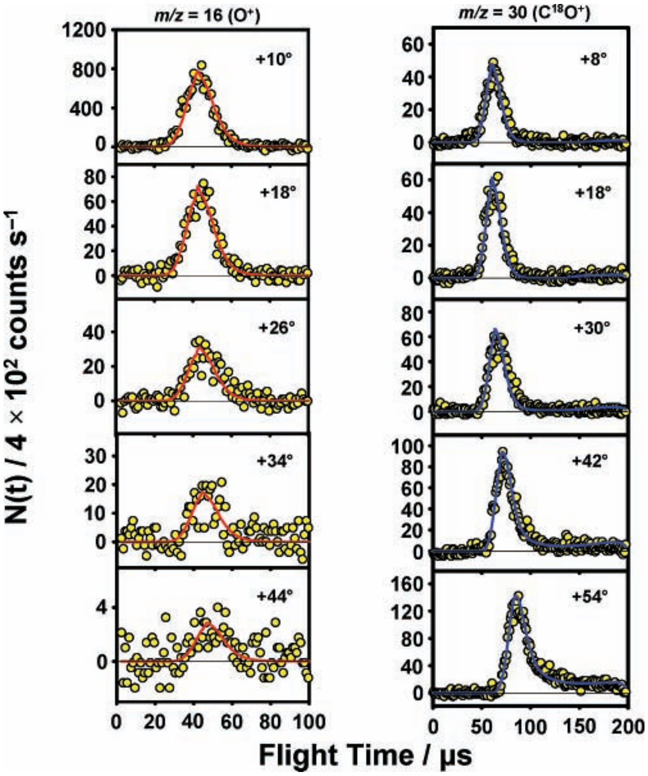

Figure 12. Time-of-flight (TOF) distributions of inelastically scattered O and C^{18}O following collisions with $\langle E_{coll} \rangle$ = 83 kcal mol^{-1}. The circles are the experimental data. The red (O) and blue (C^{18}O) solid curves are the forward-convolution simulations of the data, derived from the c.m. angular and translational energy distributions of corresponding colors in Figure 14.

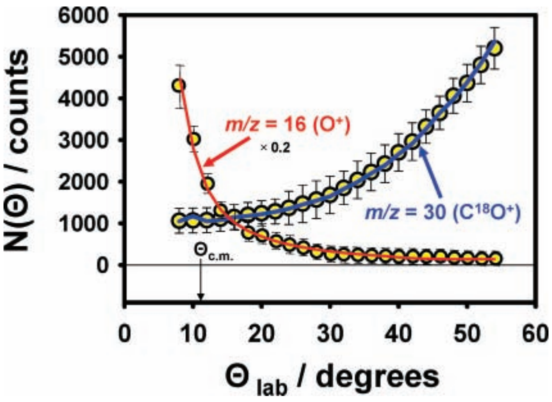

Figure 13. Laboratory angular distributions of O atoms and C^{18}O molecules that scattered inelastically with $\langle E_{coll} \rangle$ = 83 kcal mol^{-1}. The circles with error bars are the experimental data, and the colored lines are the forward-convolution fits to the data, derived from the c.m. angular and translational energy distributions of corresponding colors in Figure 14. The error bars are estimated from fitting the experimental TOF distributions with a modified Gaussian function and finding areas of the maximum and minimum acceptable fits by adjusting the Gaussian parameters. The error bars thus represent the maximum and minimum integrals of the TOF distributions based on our best judgment and are expected to be greater than ±2σ.

signals combined with high background levels of H_2O in the detector at $m/z = 18$ made it impossible to detect the reactive ^{18}O product. TOF distributions were collected for 1000 beam pulses for $m/z = 28$ (^{16}OC$^+$) and 30 (C^{18}O$^+$) and 200 beam pulses for 16 (O$^+$), and 32 (O_2^+) at each laboratory angle. The laboratory angle was adjusted in 2° increments until the entire angular range was covered. Then the increment direction was reversed and the cycle was repeated until a total of four TOF distributions had been collected for each product at each detector angle. Because this process lasted more than 35 h, it was important to sum the TOF distributions collected in this manner to account for minor long-term drifts in the experimental parameters. At a representative laboratory angle of 10°, the integrated count rates were 8.5×10^6 counts s^{-1} for $m/z = 30$ (C^{18}O$^+$), 1.2×10^8 counts s^{-1} for $m/z = 16$ (O$^+$), and 2.5×10^7 counts s^{-1} for $m/z = 28$ (^{16}OC$^+$).

III.B. Experimental Results. *III.B.1. Inelastic Scattering.* Figure 12 shows TOF distributions for $m/z = 16$ (O$^+$) and 30 (C^{18}O$^+$) collected at five representative laboratory detector angles. Figure 13 shows laboratory angular distributions for inelastically scattered ^{16}O and C^{18}O. The curves in Figures 12 and 13 are the forward-convolution fits to the laboratory angular distributions for the ^{16}O product (red) and the C^{18}O product (blue), based on the c.m. translational energy and angular distributions in Figure 14. The distributions shown in Figure 14 are taken from the theoretical results in Figures 2 and 3 but presented on a linear scale. These calculated c.m. distributions accurately predict the laboratory distributions, as seen in Figures 12 and 13. The ^{16}O product is forward scattered and the C^{18}O is backward scattered with respect to the initial direction of the reagent ^{16}O atoms in the c.m. frame. The laboratory detection angles are primarily sensitive to C^{18}O molecules that scatter into the backward hemisphere in the c.m. reference frame with respect to the direction of the incident C^{18}O molecules (see Figure 11), so only the angular range in the c.m. angular distributions that was accessible in the experiment was used in the forward convolution. The experiments were sensitive to C^{18}O and ^{16}O scattered from 0° to 120° and from 0° to 80°, respectively, in the c.m. reference frame. The translational energy distribution reveals that, on average, about 85% of the available energy (83 kcal mol^{-1}) is released in translation in the inelastic channel, although there is a tail to low translational energies suggesting that some collisions result in large energy transfers to internal degrees of freedom of C^{18}O. The angular

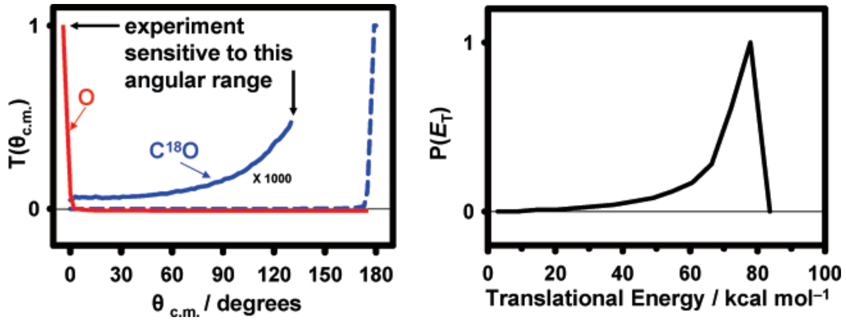

Figure 14. Center-of-mass (c.m.) angular and translational energy distributions for the inelastic scattering of O with $C^{18}O$ at $\langle E_{coll} \rangle = 83$ kcal mol^{-1}, used in the forward-convolution fit of the laboratory TOF and angular distributions for $m/z = 16$ (O^+) and 30 ($C^{18}O^+$). These distributions were obtained from QCT calculations for O (red) and $C^{18}O$ (blue).

distributions of scattered ^{16}O and $C^{18}O$ illustrate the propensity for forward scattering, which results from high-impact-parameter collisions.

Although the hyperthermal beam in our experiment had only 2% O_2, the inelastic cross section for $O_2 + C^{18}O$ is almost twice that for $O + C^{18}O$, so the contribution to the inelastic scattering signal detected at $m/z = 30$ ($C^{18}O^+$) was not beneath our detection limits. A second inelastic scattering process, $O_2 + C^{18}O \rightarrow C^{18}O + O_2$ was identified as a small, fast shoulder in the TOF distributions collected at $m/z = 30$ ($C^{18}O^+$). A functional form for the fast component was determined, and this component was subtracted from all the TOF distributions collected at $m/z = 30$ ($C^{18}O^+$), including those shown in Figure 12. Only the slower (main) peak, corresponding to the $C^{18}O$ that scattered inelastically from ^{16}O, was used to gather dynamical information about the inelastic channel.

III.B.2. Reactive Scattering. TOF distributions collected at $m/z = 28$ ($^{16}OC^+$) at five representative laboratory angles are shown in Figure 15, and the corresponding laboratory angular distribution is shown in Figure 16. Center-of-mass angular and translational energy distributions for the $^{16}O(^3P) + C^{18}O \rightarrow {}^{16}OC + {}^{18}O$ reaction were obtained from the QCT calculations and are shown as dashed blue curves in Figure 17. These c.m. distributions were used in the forward-convolution procedure to predict laboratory TOF and angular distributions shown as dashed blue curves in Figures 15 and 16. The TOF distributions, predicted from the theoretical c.m. translational energy and angular distributions, match the experimental distributions very well, but the predicted laboratory angular distribution does not quite match the observed flux difference between forward and sideways scattering in the laboratory angular distribution. The experimentally derived ("best-fit") c.m. translational energy and angular distributions are shown as red curves in Figure 17. These experimental curves were obtained by optimizing a translational energy distribution, based on an RRK form,[19] and an angular distribution of arbitrary point form. The corresponding laboratory TOF and angular distributions are shown as the solid red curves in Figures 15 and 16. The theoretically calculated translational energy distribution exhibited some structure, but the experimental resolution did not justify adding structure to the experimentally derived translational energy distribution. Thus, within experimental error, both the theoretical and experimental translational energy distributions may be the same. The difference between the theoretical and experimental c.m. angular distributions is believed to be just outside experimental error. The theoretical and experimental results both indicate that about 60% of the available energy is released in translation and that the ^{16}OC product is predominantly forward scattered. The theoretical calculations predict a small increase in the amount of ^{16}OC scattering at the most backward angles, near 180°, but that angular range is beyond the range to which the experiment is sensitive. A velocity-flux map, shown in Figure 18, illustrates the differential scattering cross section of the reactive ^{16}OC product, where ^{16}OC tends to be forward scattered, with a broad range of product velocities. In the angular range probed by the experiment, the theoretical and experimental results for this channel are in almost quantitative agreement, with only a slight discrepancy in the angular distribution.

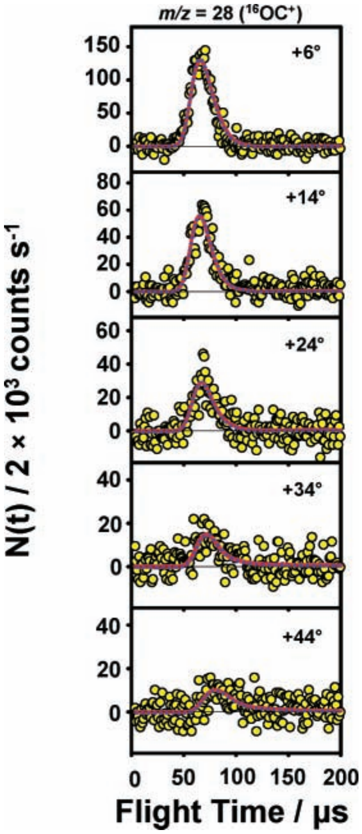

Figure 15. Time-of-flight (TOF) distributions of reactively scattered ^{16}OC following reaction of $O(^3P)$ with $C^{18}O$ at $\langle E_{coll} \rangle = 83$ kcal mol^{-1}. The circles are the experimental data. The dashed blue and solid red curves are the forward-convolution simulations of the data, derived from the c.m. angular and translational energy distributions of corresponding colors in Figure 17. The dashed blue curves are predicted by theory, and the solid red curves are the results from optimizing the c.m. distributions (shown in Figure 17) to fit the data. The experimental (solid red) and the theoretical (dashed blue) curves are nearly identical for each TOF distribution.

IV. Discussion

The experimentally observed inelastic scattering data is predicted quantitatively by the theoretical c.m. translational

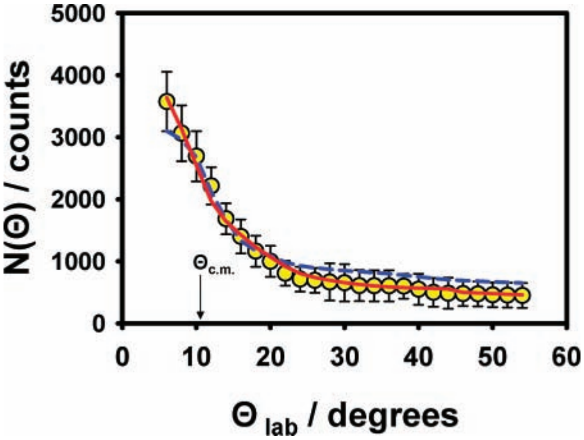

Figure 16. Laboratory angular distribution (circles with error bars) of the reactively scattered ^{16}OC product following reaction of O(^{3}P) with C^{18}O at $\langle E_{coll} \rangle = 83$ kcal mol^{-1}. The dashed blue and solid red curves are the forward-convolution simulations of the data, derived from the c.m. angular and translational energy distributions of corresponding colors in Figure 17. The dashed blue curve is predicted by theory, and the solid red curve is the result from optimizing the c.m. distributions (shown in Figure 17) to fit the data. The error bars are estimated from fitting the experimental TOF distributions with a modified Gaussian function and finding areas of the maximum and minimum acceptable fits by adjusting the Gaussian parameters. The error bars thus represent the maximum and minimum integrals of the TOF distributions based on our best judgment and are expected to be greater than $\pm 2\sigma$.

energy and angular distributions. As expected for inelastic collisions, ^{16}O atoms scatter from C^{18}O with little change in direction and velocity. Thus, the ^{16}O atoms are predominantly forward scattered and the C^{18}O molecules are predominantly backward scattered in the c.m. reference frame. And the c.m. translational energy distribution has a maximum near the c.m. collision energy. Subtracting the translational energy distribution from the collision energy gives the internal energy distribution of scattered C^{18}O. On average, ~15% of the collision energy is transferred into internal energy. However, the low-energy tail in the translational energy distribution indicates that a large fraction (~84%) of single ^{16}O(^{3}P) + C^{18}O collisions can transfer more than ~6 kcal mol^{-1} into internal energy in C^{18}O, corresponding to greater than one quantum of vibration ($v = 1$). A smaller fraction (~0.5%) of scattered C^{18}O molecules may have more than ~63 kcal mol^{-1} of internal energy, corresponding to C^{18}O ($v = 11$). Although the majority of inelastic collisions lead to C^{18}O that is scattered in the backward direction with respect to the initial direction of the reagent O atoms, it should be noted that C^{18}O detected in the experiment can only come from collisions of ^{16}O atoms with C^{18}O molecules that lead to C^{18}O scattering in the forward direction with respect to the direction of the reagent ^{16}O atoms (refer to Newton diagram in Figure 11). The forward-scattered C^{18}O is likely to be the result of low-impact-parameter collisions. Large energy transfers have been observed when hyperthermal Ar atoms scatter from C$_2$H$_6$ or C$_2$F$_6$ at low impact parameters;[15,24] however, in analyzing the calculated O + CO trajectories, it was difficult to conclude that low-impact-parameter collisions were necessarily correlated with large energy transfers. Instead, large energy transfers in inelastic collisions seem to be correlated with failed reactive collisions (see below).

An analysis of the experimental results suggests that roughly 10% of the collisions of ^{16}O(^{3}P) with C^{18}O at $\langle E_{coll} \rangle = 83$ kcal mol^{-1} lead to an O-atom exchange reaction, detected by the observation of scattered ^{16}OC. Assuming a typical hard-sphere cross section of ~10^{-15} cm^2, this experimental result would suggest a total reactive cross section, $\sum_{i=0} \sigma^r(v = i)$, of ~10^{-16} cm^2. This value is in rough agreement with the present QCT calculated total reactive cross section of 1.98×10^{-16} cm^2. As the photon excitation functions computed here are about an order of magnitude larger than those reported earlier by Upschulte and Caledonia[5] and Green et al.,[6] the consistency of the present theoretical and experimental results suggests that the cross sections of refs 5 and 6 are in fact too low.

The theoretically calculated and experimentally derived c.m. translational energy distributions for reactive collisions (see Figure 17) agree within experimental uncertainty, suggesting a broad range of product translational energies with an average of 60% of the available energy (i.e., the collision energy) released in translation. The theoretically calculated c.m. angular distribution is very similar to the experimentally derived angular distribution (see Figure 17), but these two distributions are not quite in quantitative agreement. The experimental result predicts slightly more forward scattering of OC relative to sideways scattering than does the theoretical result. The slight disagreement in the c.m. angular distributions might reflect a minor error in the OCO potential or, perhaps, the fact that the calculations employed a classical rather than quantum scattering treatment. The good agreement between the experimental results and the predictions of the QCT calculations, which used only the three low-lying triplet potential energy surfaces, suggests that ISC does not play an important role in the dynamics of O(^{3}P) + CO collisions. The absence of ISC was also a conclusion in the measurements of the excitation functions for O(^{3}P) + H$_2$ → OH + H,[25] and O(^{3}P) + CH$_4$ → OCH$_3$ + H,[9] and in the dynamics of the reaction O(^{3}P) + D$_2$ → OD +D.[8] The c.m. translational energy distributions show that reactively scattered OC tends to be highly internally excited. On average, the reactive OC products are formed with internal energies corresponding to roughly $v = 5$ or $v = 6$. But a significant fraction (~8%) are formed with internal energies corresponding to $v = 11$ or higher.

The propensity of reactive OC products to scatter in the forward direction might be interpreted as a manifestation of a stripping reaction, in which the reaction occurs through high-impact-parameter collisions. A spectator stripping limit may be quantified by the ratio of reduced masses of the pairwise collision system (O + C) and the total collision system (O + CO), which corresponds to the ratio between the respective c.m. collision energies. Thus, the pairwise reaction may be regarded as an association reaction with full conversion of the pairwise collision energy into internal excitation. This analysis would predict ~67% (~61% for O + C^{18}O) of the collision energy converted into internal excitation, while ~33% (~39% for O + C^{18}O) would be converted into translation. The experimental and theoretical c.m. translational energy distributions (Figure 17) have maxima at approximately 40% of the available energy, in apparent agreement with the spectator stripping limit.

Examination of the calculated trajectories, however, suggests that the O-atom exchange reaction does not generally follow a spectator stripping mechanism. Several examples of animated trajectories may be viewed online as Supporting Information. With the exception of the large-impact-parameter collisions that lead to inelastic scattering with little change in direction and velocity, the collisions that lead to both inelastic and reactive products have a striking similarity. This was shown earlier in the extremely high degree of similarity of the theoretically calculated angular and translational energy distributions for the inelastic and reactive channels without the CO($v = 0$) contribution.

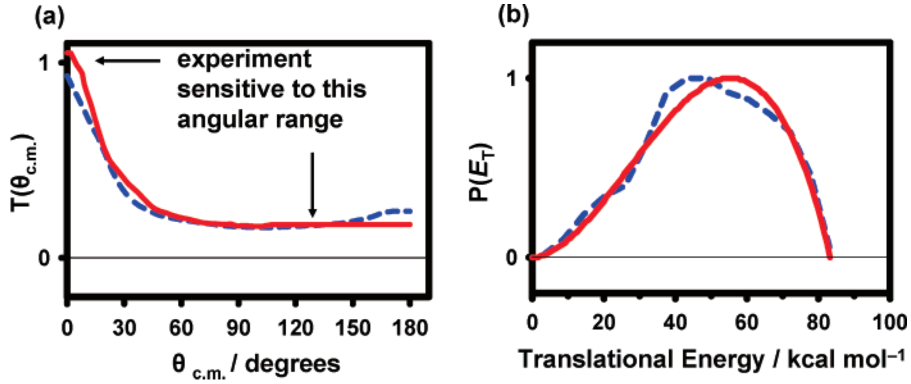

Figure 17. Center-of-mass (c.m.) angular and translational energy distributions for reactive scattering of O(^{3}P) with C^{18}O at $\langle E_{\text{coll}} \rangle = 83$ kcal mol^{-1}, used in the forward-convolution fit of the laboratory TOF and angular distributions for $m/z = 28$ (^{16}OC$^+$). The angular distribution (left) pertains to the reactively scattered ^{16}CO. The distributions shown in dashed blue were obtained from QCT calculations, and those shown in red were determined by optimizing the c.m. distributions to fit the data.

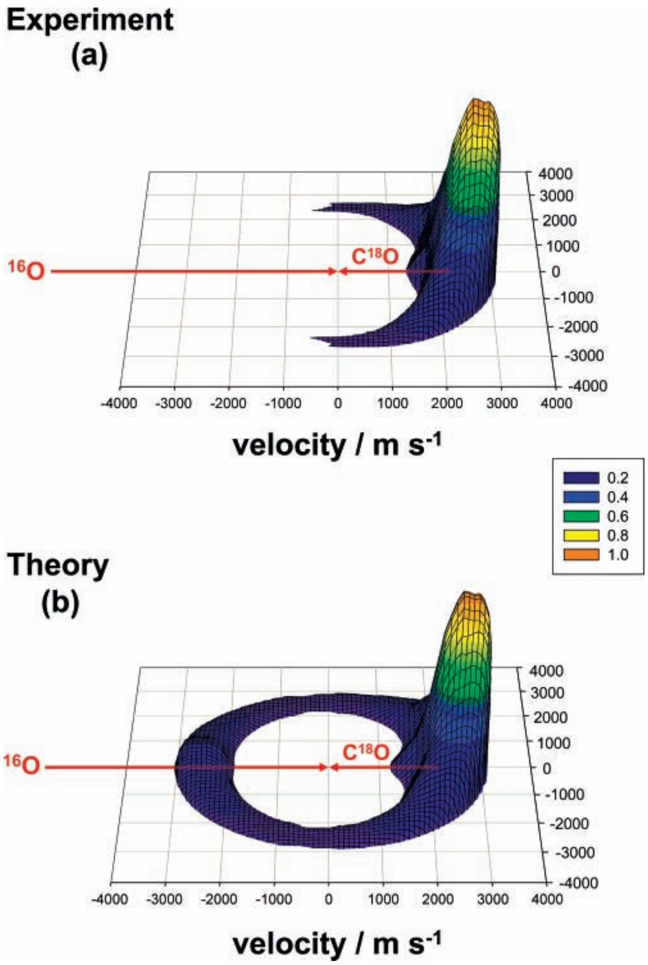

Figure 18. (a) Experimental and (b) theoretical c.m. velocity-flux maps for the reactive ^{16}OC product, derived from the angular and translational energy distributions shown in Figure 17. In each plot, the maximum flux is normalized to 1.0. Note that the experiment was not sensitive to backward-scattered ^{16}OC, so no flux appears in the backward angles in (a) even though such scattering surely occurs.

Based on examination of the trajectories and potential surfaces for vibrationally excited products formed on the two lowest potential energy surfaces, we believe that a collision complex is formed after the incoming O atom collides with CO at angles between 80° and 140° (see Figure 13 of ref 7) and strikes the repulsive wall near the carbon atom. The O atom rebounds, and an O−C−O complex is formed, moving in a quasi-bound, probably symmetric-stretch-like, mode for one or a few periods. The vibrationally excited complex, with energy far above the bound O−C−O wells, then falls apart along an unbound asymmetric-type mode. By this time, the identity of the incoming O atom has been lost, and vibrationally excited CO products are formed in about equal amounts in reactive and nonreactive (inelastic) channels. The extent of vibrational excitation and its energy dependence depend on the shapes of the repulsive walls near O−C−O symmetric stretch type geometries and on the shallowness of the O-atom approach path. A higher collision energy increases the acceptance angle over which the O atom comes close enough to the CO to react or efficiently excite CO vibrations through inelastic collisions. Thus, the reactive and inelastic cross sections increase with collision energy.

The complex can persist for several vibrational periods, but it usually does not last long enough for a rotational period. Once the complex is formed, the outcome may be an exchange of the O atom that is bound to the C atom (reactive scattering) or no exchange (inelastic scattering). Such a complex trajectory that results in inelastic scattering may be thought of as a failed reactive collision. Thus, for reactive scattering trajectories and for inelastic scattering trajectories that transfer significant energy to the CO product, the collisions involve a complex that tends to channel CO products into the forward direction but that can also fling CO products into the sideways and backward directions. The details of how the complex falls apart determine whether or not the outcome is reactive or inelastic and how the energy is partitioned into product degrees of freedom.

The shallow wells in the first two electronic states probably do not play a direct role in the dynamics at the high collision energies considered here, but they exist in a part of the potential energy surface critical for the dynamics, especially complex formation. For the reactive and inelastic channels, the two lowest electronic states yield fairly similar product CO vibrational distributions. We have not investigated the trajectories of the highest-lying electronic state to confirm the existence of complex formation on this surface. The highest-lying electronic potential energy surface is much more repulsive than the other two, and its dynamics are different. This surface has a smaller reactive cross section, and its inelastic cross section for vibrationally excited products is relatively small. The reactive CO products do not form highly excited CO. Further detailed analysis of the trajectories on the various potential energy surfaces would be required to expand our understanding of the role of complex formation on the three different electronic states.

The theoretical calculations provide a detailed view of the rotational and vibrational excitation in the CO products. Figure

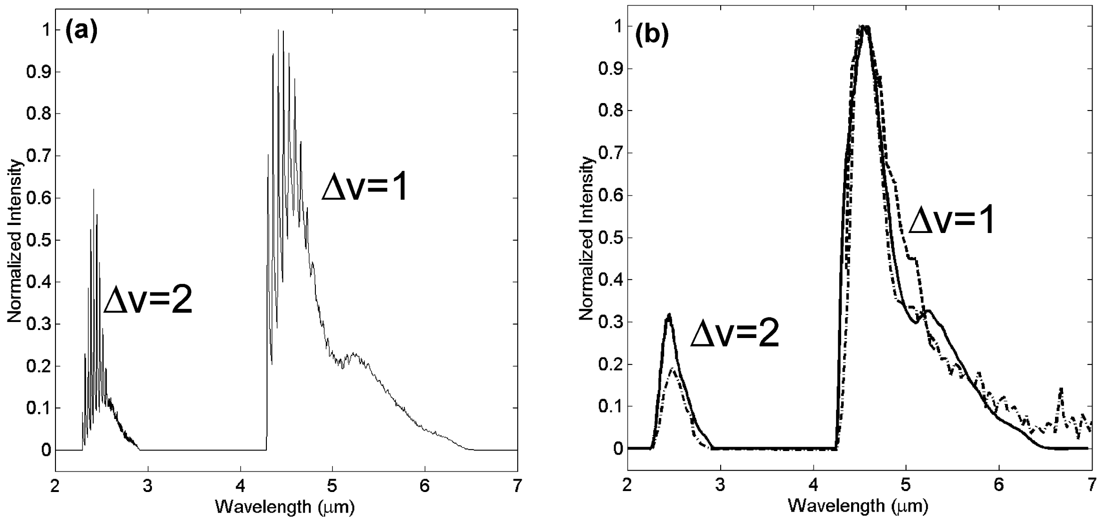

Figure 19. Infrared emission spectra from nascent CO after hyperthermal O + CO collisions. (a) Calculated spectrum at 5 cm^{-1} spectral resolution for collisions at 8 km s^{-1} collision velocity (E_{coll} = 77.9 kcal mol^{-1}). (b) (—) Calculated spectrum as in (a) degraded to 0.05 μm spectral resolution; (− · −) measured spectrum from Green et al. (ref 6); (− − −) measured spectrum of Upschulte and Caledonia (ref 5). The spectrum of Green et al. (ref 6) has been shifted by +0.0772 μm, and the spectrum of Upschulte and Caledonia (ref 5) has been shifted by −0.0848 μm. All spectra are normalized so that the maximum intensity value is 1.0.

5 shows that the reactive and inelastic rovibrationally resolved cross sections extend to $j \sim 100$. The $\sigma(0, j)$ inelastic cross section peaks at much lower rotational quantum numbers and has a much larger magnitude, reflecting the different dynamics of pure rotational excitation, which occurs at large impact parameters. The maxima for the inelastic $\sigma(v = 1{-}3, j)$ cross sections occur for lower rotational quantum numbers as the vibrational levels increase, reflecting the fact that less energy is available for rotation as the vibrational excitation increases. This trend is in agreement with previous experimental studies of reactive triatomic collisions[26] and for experimental[27] and theoretical studies[28,29] on inelastic triatomic collisions. In general, products can be highly rotationally excited, especially when the product vibrational energy is relatively low.

As an independent validation of the calculated rovibrational distributions, we show in Figure 19 calculated nascent emission spectra based on the CO(v, j) populations for the summed reactive and inelastic channels and measured nascent spectra for O + CO collisions near 8 km s^{-1} relative velocity. The calculated spectra were generated from the combined inelastic and reactive CO(v, j) populations and tabulated lifetimes for CO(v, j) states. Figure 19a shows the calculated results at 5.0 cm^{-1} resolution from 2 to 7 μm, where $\Delta v = 1$ (fundamental) and $\Delta v = 2$ (overtone) bands are clearly visible. We note the bandhead structure in the fundamental and overtone spectra corresponding to R-branch transitions from high rotational levels ($j = 50{-}100$) in excited vibrational levels of CO. Within the fundamental band, each peak corresponds to an R-branch transition from a particular vibrational level, with the shortest wavelength peak corresponding to transitions from $v = 1$, and so on. Figure 19b shows the same calculated nascent spectra degraded to 0.05 μm spectral resolution. Figure 19b also shows results from two measurements, the crossed-beams laboratory measurements of Upschulte and Caledonia,[5] which range from 4.5 to 5.5 μm, and the space-based orbital gas release measurements of Green et al.[6] (digitized from Figure 12, 17 933 scan), which range from 2 to 7 μm. The Green et al. spectra capture the fundamental and overtone emission. All spectra have been normalized so that their maxima are 1.0. The spectrum of Upschulte and Caledonia was shifted by −0.0848 μm and the spectrum of Green et al. was shifted by +0.0772 μm. There is very good agreement between all spectra for the fundamental band, except at longer wavelengths where the spectrum of Green et al. has apparently a low signal-to-noise ratio. The ratio of the overtone to the fundamental peak heights for the calculated spectrum is about 1.5 larger than the measured spectrum of Green et al. This difference may be the result of uncertainties in combining spectra from two different circular variable filters (CVFs) covering different wavelength regions (0.7−5 and 4.7−22 μm), uncertainties involving the absolute determination of relative velocities of O and CO, the sensitivity of the measured spectrum to the direction of the CVF field of view, other factors in these difficult space measurements, or in deficiencies in the present calculations. More highly resolved spectra are required to determine the origins of these differences.

The current experimental and theoretical results reveal similar limits in the amount of internal excitation in scattered CO to what was reported in the IR emission experiment conducted by Upschulte and Caledonia.[5] They concluded that collisions of O(^{3}P) with CO at E_{coll} = 77.9 kcal mol^{-1} can produce CO in vibrational levels up to $v = 11$, whereas our crossed-beams study of ^{16}O(^{3}P) with C^{18}O at $\langle E_{\text{coll}} \rangle$ = 83 kcal mol^{-1} verified that both the inelastic product, C^{18}O, and the reactive product, ^{16}OC, may be in vibrational levels of $v = 11$ or greater. A high degree of consistency is emerging between the present measurements, the spectral measurements of Caledonia and Upschulte, the spectral measurements of Green et al., and the theoretical calculations, especially with regard to the high degree of internal excitation of the product CO.

V. Concluding Remarks

Crossed molecular beams methods and theoretical calculations have been used to investigate the hyperthermal interactions of O(^{3}P) with CO at c.m. collision energies near 80 kcal mol^{-1} (corresponding to a relative velocity near 8 km s^{-1}). Inelastic scattering experiments on the process, ^{16}O(^{3}P) + C^{18}O(v, j) → C^{18}O(v', j') + ^{16}O, indicate that oxygen atoms mainly scatter from C^{18}O with relatively large impact parameters and lead to forward scattering with little change in direction and translational energy. Averaged over all inelastic collisions, ~15% of the collision energy is transferred to internal energy in CO. Although this fraction is relatively small, the collision energy is high, so internal excitation of CO above an energy corresponding to $v = 1$ still occurs in approximately 84% of all inelastic collisions. The reactive channel, $^{16}O(^3P) + C^{18}O \rightarrow {}^{16}OC + {}^{18}O$, created ^{16}OC products that are scattered mainly in the forward direction, while a minority of collisions lead to ^{16}OC scattered in the sideways and backward directions. The ^{16}OC product formed in the reactive channel had a very broad translational energy distribution, with ~40%, on average, of the available (collision) energy transferred into internal excitation. Approximately 97% of reactive collisions produce ^{16}OC with internal energies greater than an energy corresponding to $v = 1$, and about 8% of collisions lead to internal energies greater than $v = 11$. QCT calculations on computed triplet potential energy surfaces are in excellent agreement with the experimental results. The calculations reveal a mechanism for large energy transfers, into both rotation and vibration, where the reagent O atom encounters the carbon end of the CO molecule with a range of impact parameters in a bent O−C−O geometry (~80−140°). The three atoms linger together for less than a rotational period but usually for more than a CO vibrational period, and the transient complex breaks up into either inelastic or reactive products. The inelastic trajectories that lead to significant energy transfer to the CO may thus be considered failed reactive collisions. The similarity in inelastic and reactive trajectories that lead to high vibrational excitation in the CO product is supported by calculated translational energy and angular distributions for reactive and inelastic collisions without the CO($v = 0$) product. These distributions, which remove contributions from purely inelastic rotational excitation, are nearly identical.

The theoretical calculations, which use a modest one-electron basis set and level of theory, have been used to predict inelastic and reactive cross sections at a variety of collision energies and to predict infrared emission spectra that compare favorably with earlier measurements. Given the accuracy with which the calculations predict the collision dynamics observed in our high-fidelity crossed-beams experiments, we expect the mechanistic insights and additional predictions offered by the theory to be accurate, too.

It is surprising that the predictions from the present level of theory match all the details of the various experimental results so well. However, at these high collision energies, the present level of theory appears to describe the important parts of the potential adequately. The QCT approach probably works well because quantum effects are small. Thus, higher levels of theory might not change the good agreement between measurements and the present modeling results. Such a picture of hyperthermal chemistry would be consistent with several recent experimental/modeling studies where surprisingly good agreement between a modest level of theory and experiment was seen (see, for example, ref 9). It could also be the case that several unrelated modeling errors are favorably canceling out for this particular chemical system at these energies, that the good agreement is accidental, and that use of higher levels of theory will yield worse comparisons with measurements. The O + CO system is small enough that much higher levels of theory can be applied to obtain new potentials and that quantum scattering approaches could perhaps be applied even at these high energies with present modeling algorithms and computer hardware. Such studies for this experimentally well-characterized system would be valuable to gauge the level of theory needed to describe hyperthermal chemistry in general.

Acknowledgment. This work was supported by the Small Business Innovative Research (SBIR) program of the Missile Defense Agency (MDA), Contract No. F04611-03-C-0015 (technical oversight from Dr. Marty Venner), by the MDA under Cooperative Agreement HQ0006-05-2-0001, and by the Department of Defense Experimental Program for the Stimulation of Competitive Research (DEPSCoR), administered by the Air Force Office of Scientific Research (Grant No. FA9550-04-1-0428). The authors acknowledge helpful technical discussions with P. Zittel and W. Dimpfl of Aerospace Corporation, G. Caledonia of Physical Sciences, Inc., and L. Bernstein of Spectral Sciences, Inc. Amy L. Brunsvold is grateful for fellowships from the Zonta Foundation and the Montana Space Grant Consortium.

Note Added after ASAP Publication. This article was published on Articles ASAP on February 22, 2008, with an error in the Figure 3 caption. The words “inelastic” and “reactive” were transposed in the fifth line. The corrected version was posted on February 26, 2008.

Supporting Information Available: Representative animated trajectories of O + CO collisions, which represent exchange of the oxygen atom that is bound to the carbon atom (reactive scattering) and collisional excitation of CO without exchange of the oxygen atom (inelastic scattering); some trajectories show the formation of a transient complex in which the three atoms linger together for a short time, usually less than a rotational period, before separating into products. This material is available free of charge via the Internet at http://pubs.acs.org.

References and Notes

(1) English, L. K. *Mater. Eng.* **1987**, *104*, 39.

(2) Hunton, D. E. *Sci. Am.* **1989**, *261*, 92.

(3) Minton, T. K.; Garton, D. J. Chemical Dynamics in Extreme Environments. In *Advanced Series in Physical Chemistry*; Dressler, R. A., Ed.; World Scientific: Singapore, 2001; Vol. 11, pp 420−489.

(4) Murad, E. *J. Spacecr. Rockets* **1996**, *33*, 131.

(5) Upschulte, B. L.; Caledonia, G. E. *J. Chem. Phys.* **1992**, *96*, 2025.

(6) Green, B. D.; Holtzclaw, K. W.; Joshi, P. B.; Burke, H. K. *J. Geophys. Res.* **1992**, *97*, 12161.

(7) Braunstein, M.; Duff, J. W. *J. Chem. Phys.* **2000**, *112*, 2736.

(8) Garton, D. J.; Brunsvold, A. L.; Minton, T. K.; Troya, D.; Maiti, B.; Schatz, G. C. *J. Phys. Chem. A* **2006**, *110*, 1327.

(9) Troya, D.; Schatz, G. C.; Garton, D. J.; Brunsvold, A. L.; Minton, T. K. *J. Chem. Phys*. **2004**, *120*, 731.

(10) Braunstein M.; Wysong, I. J. Direct Simulation Monte Carlo Modeling of High Energy Chemistry in Molecular Beams: Chemistry Models and Flowfield Effects. Presented at the 22nd International Rare Gas Dynamics Conference, Sydney, Australia, July, 2000.

(11) Inn, E. C. Y.; Watanabe, K.; Zelikoff, M. *J. Chem. Phys.* **1953**, *21*, 1648.

(12) Schmidt, M. W.; Baldridge, K. K.; Boatz, J. A.; Elbert, S. T.; Gordon, M. S.; Jensen, J. H.; Koseki, S.; Matsunaga, N.; Nguyen, K. A.; Su, S. J.; Windus, T. L.; Dupuis, M.; Montgomery, J. A. *J. Comput. Chem.* **1993**, *14*, 1347.

(13) Aguado, A.; Paniagua, M. *J. Chem. Phys.* **1992**, *96*, 1265.

(14) Truhlar, D. G.; Muckerman, J. T. *Atom−Molecule Collision Theory*; Plenum Press: New York, 1979.

(15) Brunsvold, A. L.; Garton, D. J.; Minton, T. K.; Troya, D.; Schatz, G. C. *J. Chem. Phys.* **2004**, *121*, 11702.

(16) Lee, Y. T.; McDonald, J. D.; LeBreton, P. R.; Herschbach, D. R. *Rev. Sci. Instrum.* **1969**, *40*, 1402.

(17) O’Loughlin, M. J.; Reid, B. P.; Sparks, R. K. *J. Chem. Phys.* **1985**, *83*, 5647.

(18) Zhang, J.; Garton, D. J.; Minton, T. K. *J. Chem. Phys.* **2002**, *117*, 6239.

(19) Buss, R. J. Ph.D. Thesis, University of California, Berkeley, 1979.

(20) Lee, Y. T. Reactive Scattering I. Nonoptical Methods. In *Atomic and Molecular Beam Methods*; Scoles, G., Ed.; Oxford University Press: New York, 1988; Vol. 1, p 553.

(21) The rotational temperature of CO in the supersonic expansion is presumably far below its temperature in the pulsed valve (300 K), although the vibrational temperature of CO in the expansion is likely to remain close to 300 K. The theoretical calculations, to which the experimental results are compared, sample initial CO rotations and vibrations from a 300 K

distribution. However, the difference between the initial rotational distributions of CO in the experiment and theory is not expected to be significant for hyperthermal collision energies relevant to the current study.

(22) Auerbach, D. J. Velocity Measurements by Time-of-Flight Methods. In *Atomic and Molecular Beam Methods*; Scoles, G., Ed.; Oxford University Press: New York, 1988; Vol. 1, p 362.

(23) A key feature of the analysis, as described in ref 8, is the assumption that over the range of center-of-mass (c.m.) collision energies resulting from the velocity spread in the oxygen atom beam, the shape of the c.m. translational energy distribution, E_{trans}, of the products remains constant. Thus, in the forward-convolution procedure, a translational energy function corresponding to the nominal collision energy is averaged over the collision-energy distribution in the experiment. At each point in the averaging process, the nominal translational energy function is shifted by the energy difference between the actual collision energy and the nominal collision energy. The c.m. translational energy distributions displayed in this paper are the distributions that correspond to the nominal collision energy (i.e., 83 kcal mol^{-1} in the experiment). This approximation breaks down if the shape of the translational energy distribution is strongly dependent on collision energy. Nevertheless, in the experiments reported here it is believed that the temporal width of the incident oxygen atom beam in the lab frame results in more uncertainty in the determination of the c.m. translational energy distributions than does the range of c.m. collision energies.

(24) Tasic, U.; Hein, P.; Troya, D. *J. Phys. Chem. A* **2007**, *111*, 3618.

(25) Garton, D. J.; Minton, T. K.; Maiti, B.; Troya, D.; Schatz, G. C. *J. Chem. Phys.* **2003**, *118*, 1585.

(26) Chapman, W. B.; Blackmon, B. W.; Nizkorodov, S.; Nesbitt, D. J. *J. Chem. Phys.* **1998**, *109*, 9306.

(27) Lindner, J.; Lundberg, J. K.; Lovejoy, C. M.; Leone, S. R. *J. Chem. Phys.* **1997**, *106*, 2265.

(28) Aker, P. M.; Valentini, J. J. *J. Phys. Chem.* **1993**, *97*, 2078.

(29) Schatz, G. C. *J. Chem. Phys.* **1997**, *106*, 2277.